



Cite this: *Nanoscale Adv.*, 2023, 5, 2973

# Exosomes trapping, manipulation and size-based separation using opto-thermo-electrohydrodynamic tweezers†

Chuchuan Hong, <sup>ab</sup> Sen Yang<sup>ab</sup> and Justus C. Ndukaife <sup>\*abc</sup>

Owing to the heterogeneity of exosomes in size and biomolecular composition, there is a need for new approaches for trapping, manipulating, and sorting of single exosomes in solution. Due to their small size ranging from 30 nm to 150 nm and their relatively low refractive index, their stable trapping using optical tweezers has been met with challenges. Trapping exosomes in an optical trap requires nearly 100 mW of input power, which predisposes them to photo-induced damage and membrane rupture at the laser focus. Here, we report a high stability opto-thermo-electrohydrodynamic tweezer for the stable stand-off trapping of single exosomes based on a concentric nanohole array (CNA) using laser illumination and an a.c. field. The CNA system generates two regions of electrohydrodynamic potentials several microns away from the laser focus where single exosomes are trapped. We demonstrate the rapid trapping within seconds, and selective dynamic manipulation of exosomes based on size using only 4.2 mW of input laser power. The proposed platform opens up a promising approach for stabilizing single exosomes in solution and controlling their distribution based on size without the risk of photo-induced damage.

Received 13th February 2023  
Accepted 3rd May 2023

DOI: 10.1039/d3na00101f

rsc.li/nanoscale-advances

## Introduction

The stable trapping of single biological particles against Brownian motion within an observation volume is crucial to understand their biophysical and biochemical properties on an individual particle level.<sup>1–7</sup> Exosomes are membrane-delimited nanoscale extracellular vesicles (EVs) secreted by cells that contain important biological information molecules including proteins, lipids and nucleic acids, and thus serve as potential biomarkers for noninvasive cancer detection.<sup>8–10</sup> They are released when multivesicular body fuses with the cell plasma membrane.<sup>11,12</sup> The ability to analyse exosomes in low concentration media using small sample volumes is important for early-stage disease detection and prognosis.<sup>13–15</sup> Also, due to the heterogeneity of exosomes both in size and biomolecular compositions,<sup>16–18</sup> the ability to achieve single exosome trapping and analysis is crucial to understanding their properties on an individual particle level. However, exosomes are very small biological particles measuring only 30 nm to 150 nm in diameter,<sup>10</sup> which results in strong Brownian motion that makes their stable trapping in solution challenging. While

conventional optical tweezers can trap and manipulate single bio-particle of micron-size, such as bacteria or cells,<sup>19,20</sup> they are unable to address nanoscale biological particles like exosomes with low optical powers due to the diffraction limit. Studies have shown that to trap single nanosized exosomes in solution with optical tweezers requires nearly 100 mW of incident power,<sup>21–24</sup> which poses the risk of irreversible photothermal damage, such as membrane rupture, photo-toxicity or thermal stress,<sup>25,26</sup> to delicate bio-particles. Plasmonic nano-tweezers, alternatively, are invented to handle nanometric particles<sup>27–31</sup> due to the tighter light confinement resulting from plasmonic resonance. One vital issue with conventional plasmonic nano-tweezers is that plasmonic resonators are always fabricated on a substrate, which prohibits dynamic manipulation of particles with the same flexibility as optical tweezers. Active colloidal tweezers have been proposed to solve this problem based on a ‘tweezer in a tweezer’ configuration.<sup>32,33</sup> However, they require complicated fabrication techniques and do not offer the same level of flexibility in the design of the plasmonic elements in comparison with lithographic fabrication. Moreover, in plasmonic nano-tweezers, the transport of particles towards the electromagnetic hotspot relies on slow and nondeterministic diffusion, making the conventional plasmonic nano-tweezers unsuitable to a low particle concentration environment. To overcome the time-consuming particle-loading challenge, electrothermoplasmonic tweezers have been demonstrated to achieve fast particle transport by taking advantage of photo-induced heating.<sup>26,34,35</sup> However, the temperature rise at the trapping site must be managed.

<sup>a</sup>Electrical and Computer Engineering Department, Vanderbilt University, Nashville, TN, 37212, USA. E-mail: justus.ndukaife@vanderbilt.edu

<sup>b</sup>Vanderbilt Institute of Nanoscale Science and Engineering, Vanderbilt University, Nashville, TN, 37212, USA

<sup>c</sup>Interdisciplinary Material Science, Vanderbilt University, Nashville, TN, 37212, USA

† Electronic supplementary information (ESI) available. See DOI: <https://doi.org/10.1039/d3na00101f>



In an earlier work, we established a safe and rapid platform for trapping single nanoscale objects in low-concentration media called opto-thermo-electrohydrodynamics-tweezer (OTET).<sup>26</sup> In the OTET platform, a nanoparticle is trapped outside a square nanohole array and is dynamically manipulated by moving laser spot on the nanohole array. In this work, we have advanced the OTET platform by tailoring the topology of nanohole array into a concentric nanohole array (CNA) pattern to create two trapping sites, namely site I and site II as shown in Fig. 1(a). In this way, we increase the trapping stability in site II, while keeping the properties of stand-off trapping, fast particle transport, and dynamic manipulation. Interestingly, we experimentally demonstrate the trapping of exosomes at different locations based on their sizes. Therefore, our new platform provides the opportunity for spatially-resolved single-exosome trapping and on-chip analysis at low-concentration levels in real time.

## Experimental

The CNA platform is composed of a 120 nm gold film on a float-glass substrate, where the gold film is patterned with a concentric nanohole array (CNA), as shown in Fig. 1(a) and (b). The inner circle has a diameter of 30  $\mu\text{m}$ , the gap size is 20  $\mu\text{m}$ , and the ring width is set to 20  $\mu\text{m}$ . The nanohole array is optimized to have a 680 nm lattice constant and 130 nm in nanohole radius, as depicted in Fig. 1(c). Large or small-size exosomes can be trapped in site I together, while small-size exosomes can be transferred into site II under certain a.c.

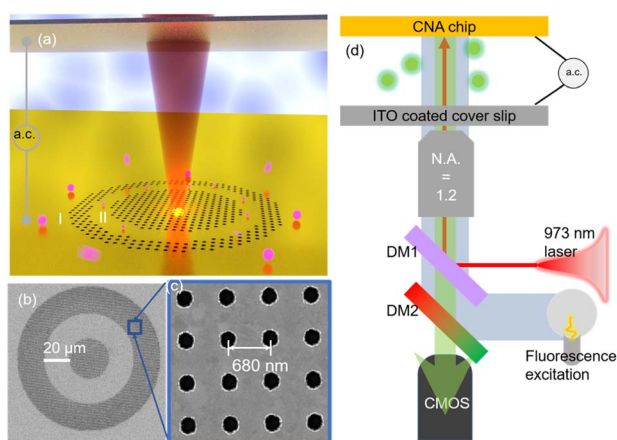


**Fig. 1** (a) Schematic illustration of concentric nanohole array (CAN) system. Laser is illuminated at the center of the CNA. a.c electric field is applied perpendicular to the gold film. Exosomes (shown in purple) are rapidly transported and trapped. Letters I and II indicate two sites available for trapping. (b) Scanning electron microscopy (SEM) image of template-stripped patterned gold film. (c) The zoomed-in image of part of the template-stripped nanohole array. (d) The experimental light path for trapping and imaging the fluorescently labeled exosomes. DM1 and DM2 are dichroic mirrors. DM1 reflects the 973 nm trapping laser towards the sample but blocks it from entering the camera. DM2 reflects the excitation of fluorescence towards the sample but only allows the emitted light to pass through and be collected by the CMOS camera.

frequencies. As depicted in Fig. 1(d), both 973 nm laser and a.c. electric field need to be switched on so that we are able to observe the trapping of fluorescently labeled exosomes. We attribute this trapping to the balance between two opposing microfluidic flows, *i.e.* a.c. electro-osmotic (ACEO) flow and electrothermoplasmonic (ETP) flow.<sup>26</sup> As shown in Fig. 1(d), an a.c. electric field is applied perpendicular to the gold film using the patterned film as one of the electrodes. The nanohole pattern distorts the applied a.c. electric field, creating tangential components near the surface of the gold film. The tangential components of electric field then exert coulombic forces on the ions and charges in the electric double layer near the gold film. The moving ions and charges form a directional fluidic motion near the surface, which is called a.c. electro-osmotic flow. This osmotic flow is moving in a direction away from the nanohole array and repels particles out of the nanohole array region.

Furthermore, an ETP flow is generated by the laser-induced heating of the nanohole array and the applied a.c. electric field. Laser illumination efficiently produces local temperature rise due to the plasmonic resonance of the nanohole array.<sup>36</sup> Fig. 2(a) shows the electric field profile at the top surface of one unit-cell of the nanohole array. It clearly shows the light field is concentrated near the fringe region of the nanohole, as well as the region in-between the nanoholes due to electromagnetic coupling. This in turn improves the photothermal conversion efficiency of the nanohole array under the 973 nm laser illumination. We also plot the simulated reflection and absorption spectrum in Fig. 2(b) to show an enhanced absorption at 973 nm. The simulated temperature profile on top of the gold film is provided in Fig. 2(c). It shows a peak local temperature rise of 24 K under a laser illumination intensity of  $3 \times 10^9 \text{ W m}^{-2}$ . We note that the temperature rises at the trapping sites I and II is negligible. Due to this thermal gradient, a body force is generated in the fluid element under the application of an a.c. electric field.<sup>37</sup> This body force drives a vortex-like fluidic motion called electrothermoplasmonic flow inside the microfluidic channel.<sup>34,38</sup> Near the gold film, the ETP flow moves towards the hot region, where the laser is illuminated. The two opposing flows, namely ETP and ACEO flows establish the stagnation zones where the in-plane velocity goes to zero, defining where the exosomes are trapped.

Fig. 2(d)–(f) illustrates the simulated in-plane microfluidic flow field distribution near the gold film surface. In Fig. 2(d), the arrows represent the total local in-plane flow (ACEO + ETP) direction. The details of the governing equations for the numerical simulations can be found in our previously published article.<sup>26</sup> As highlighted in the red box (labeled site I), the opposing inward ETP and outward ACEO flows meet and create the stagnation zone outside the CNA pattern. The highlighted yellow box (labeled site II) indicates the existence of another available trapping position besides site I. Since site II is sandwiched by two nanohole arrays, particles at site II experience the ACEO flows coming from both the inner and outer nanohole array as well as the inward ETP flow. Fig. 2(e) and (f) show the 2D simulated in-plane total flow velocities *versus* radial distance for both trapping sites II and I, respectively, with the radially



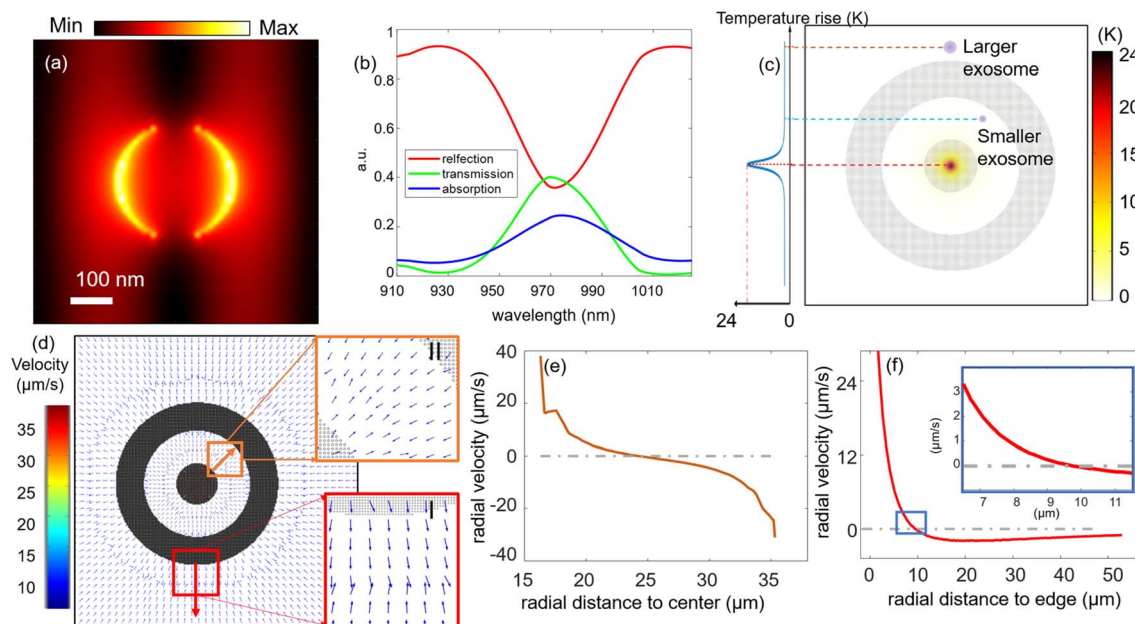


Fig. 2 (a) Simulated electric field profile on top of one unit-cell of the nanohole array using Finite-Difference Time-Domain (FDTD) method. (b) The simulated transmission, reflection and absorption spectrum of the optimized nanohole array. (c) The simulated temperature rises when illuminating a 973 nm laser at the center of CNA. Laser spot is 1.33  $\mu\text{m}$ . (d) The total in-plane velocity map of CNA system. It clearly shows two possible trapping sites where the in-plane velocity arrows are pointing oppositely, labeled as I and II. The orange arrow and red arrow indicate the trajectory where we plot out the in-plane velocity as shown in (e) and (f). (e) and (f) Simulated in-plane velocity in trapping site II and trapping site I, corresponding to the orange and red arrows in (d), respectively. Positive velocity is defined as velocity direction pointing away from the center. Inset in (f) plots a zoomed-in version of the blue box, to show the position of the stagnation zone.

outward direction defined as positive. The radial positions where the velocities go to zero in Fig. 2(e) and (f) depict the stagnation zones, which correspond to the trapping positions. The confinement along the out-of-plane direction is because of the particle–surface interaction, which describes the attractive force between the surface charge on a particle close to the surface and its image charge inside the conducting film.<sup>39</sup>

For the experimental demonstrations, we adapted a combination of electron beam lithography and the template stripping method<sup>40,41</sup> to fabricate the patterned gold film. The detailed fabrication process is provided in the ESI† section. The fabricated gold film was then covered by an Indium–Tin–Oxide (ITO) coated glass cover slip but separated by a dielectric spacer (120  $\mu\text{m}$ ) to create a microfluidic channel. Subsequently, diluted exosome solution was injected into the microfluidic channel using a syringe. A 973 nm wavelength laser is focused onto the center of the CNA using a water-immersion objective lens (60 $\times$ ) with a numerical aperture of 1.2. Alternating current (a.c.) electric voltage is applied across the microfluidic channel to give a field strength of 83 333  $\text{V m}^{-1}$ .

The experimental demonstration of trapping single exosomes is conducted using diluted commercial FITC-conjugated exosomes solution (Creative Diagnostics). The final concentration of exosomes is diluted to  $1.8 \times 10^5$  particles per mL. Fig. 3(a) shows a frame-by-frame sequence of the rapid transport, trapping, sorting and spatially-resolved size-based separation of exosomes. Starting from a vacant system with a laser spot focused at the center and the a.c. electric field being off, no

exosome is observed to be trapped. Immediately after the a.c. field is turned on at a frequency of 1.5 kHz, exosomes are rapidly transported by ETP flow to site I and trapped within 2 seconds. Due to the low a.c. frequency field of 1.5 kHz, the radially outward ACEO flow in the CNA is strong enough to preclude exosomes from entering site II. Thus, at this frequency, all the exosomes are trapped at the external periphery of the CNA system (namely site I). Subsequently, the a.c. frequency is tuned up to 3.5 kHz and the smaller exosomes (circled in blue) are observed to hop into the gap, *i.e.* site II. The a.c. frequency is kept at 3.5 kHz for 3 seconds to ensure all the small exosomes transit the barrier, hopping from site I to site II. By so doing, the CNA system enables the spatially-resolved sorting of bio-particles, ensuring that smaller and larger exosomes are separated and trapped at different locations. We also note that in general the trapping stability of site II is higher than in site I as depicted in Fig. 3(e). Finally, the a.c. frequency is reduced to 2 kHz and the particles remain trapped at the respective positions. The release of the trapped exosomes can be achieved by increasing the frequency to 10 kHz or more.<sup>26</sup> To confirm the size of the trapped exosomes, we applied a low frequency a.c. field of 10 Hz a.c. to immobilize all trapped exosomes onto the substrate.<sup>34</sup> Subsequently, the sample is imaged under a scanning electron microscopy (SEM) system. The SEM image is provided in Fig. 3(b) and (c). We thus verified that the exosome in site II has a diameter of around 60 nm, while a larger exosome with a diameter of about 120 nm was trapped in site I.



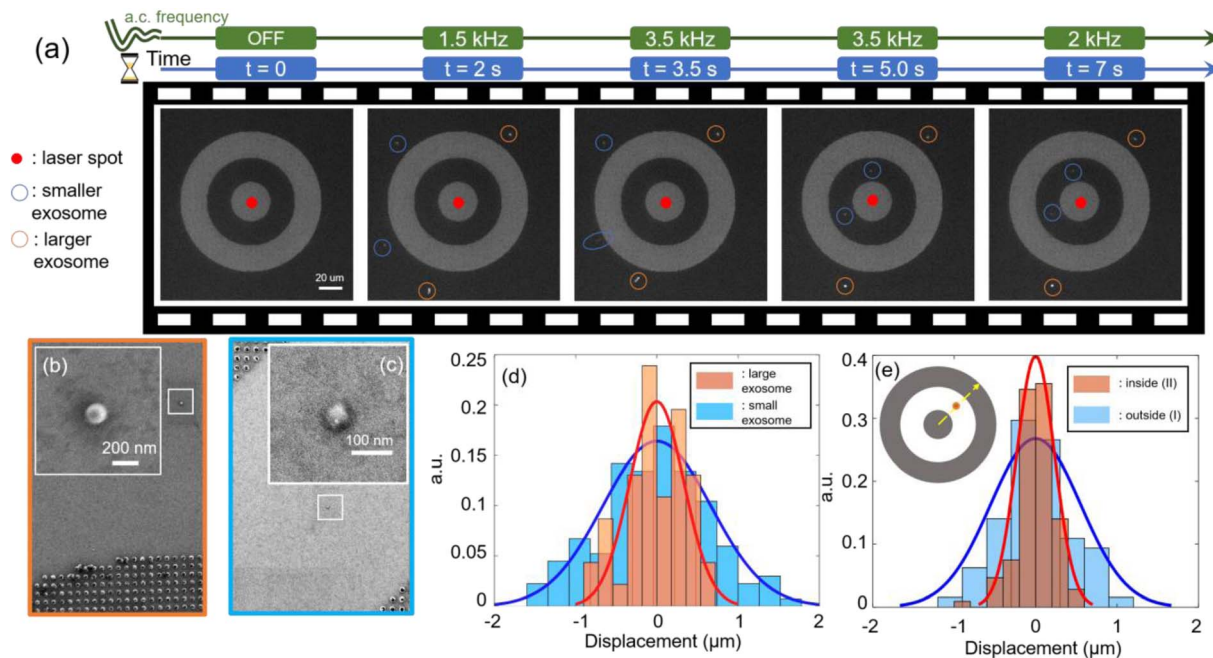


Fig. 3 (a) The frame-by-frame illustration of rapidly transporting and trapping individual exosomes. Then by tuning a.c. frequency, we achieved size-based exosomes sorting and trapping at different locations. (b) and (c) are the SEM images of exosomes trapped in site II and I, respectively, after we pattern the exosomes onto gold film using ultra-low frequency a.c. field. SEM images confirm the size-based separately trapping. (d) Histograms of radial position displacement of trapped small-size and larger-size exosomes under 3 kHz a.c. frequency. (e) Histograms of radial position displacement when the same small-size exosome is trapped outside the CNA or inside the gap, under the same 2 kHz a.c. frequency. The stability is enhanced at site II. The inset indicates the definition of radial direction in the analysis of (d) and (e), (yellow arrow).

## Methods

### Sample preparation

After the CNA chip was fabricated, we sandwiched the gold film by covering it with an ITO-coated glass cover-slip, spaced by a 120  $\mu\text{m}$ -thick dielectric spacer to create a microfluidic channel. Two copper wires are connected to the ITO side on the cover-slip and the gold film, respectively, to apply the a.c. electric field.

The FITC-conjugated fluorescently-labeled exosomes were purchased from Creative Diagnostics as lyophilized particles. 100  $\mu\text{l}$  DI water was added to 100  $\mu\text{g}$  of solid and mixed well to obtain a concentration of 1 mg per mL exosome solution. The concentration is  $\sim 10^{10}$  exosomes per mL as suggested by the instruction. The acquired exosome solution was then diluted to  $1.8 \times 10^5$  exosomes per mL by adding more DI water.

### Fluorescence imaging

The trapping experiment and fluorescence imaging were conducted on Nikon Ti2-E inverted microscopic system. The detailed light path is presented in Fig. 1(d) in the main text. A high quantum efficiency sCMOS camera (Photometrics PRIME 95B) was used to acquire images at 5 frames per second. The labeled exosomes were excited under blue light filtered out from a broadband fluorescent illumination lamp (Nikon INTENSILIGHT C-HGFI). The emitted light was collected through the same objective lens and imaged on the camera. The nanohole array was illuminated with a 973 nm semiconductor diode laser

(Thorlabs CLD1015). The laser beam was focused with a Nikon  $\times 60$  water-immersion objective lens (NA, 1.2). The a.c. electric field was supplied by a dual-channel function generator (BK Precision 4047B).

## Results and discussion

To interpret the mechanism of this size-based sorting, as well as emphasize the high trapping stability in site II, we consider the relationship between trapping stability with respect to the applied a.c. frequency. For a low a.c. frequency of 1.5 kHz, the ACEO is strong enough to balance the ETP flow outside the nanohole array. Furthermore, the particle-surface interaction force ( $F_s$ ) is stronger at lower a.c. frequencies, and as a result, both large and small exosomes are transported by the ETP flow and trapped at site I. As the a.c. frequency is increased to 3.5 kHz, both the ACEO flow strength and particle-surface interaction force is reduced, while the ETP flow strength is relatively unchanged. This lowers the trapping stability in site I. As evident in Fig. 3(d), it is shown that the smaller exosomes experience a lower trapping stability than the larger exosomes under a 3 kHz frequency since they experience a larger Brownian motion. As the a.c. frequency increases to 3.5 kHz, the trapping stability is sufficiently reduced such that the smaller exosomes at site I are released and transported inward to site II where they become trapped. The smaller exosomes are stably trapped at site II because site II has a larger trapping potential well depth than site I. The experimental data shown in Fig. 3(e)



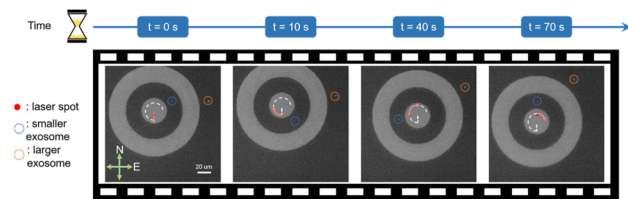


Fig. 4 The frame-by-frame sequence of selective dynamic manipulation on the trapped small size exosome in site II using the move of laser, while the large exosome trapped outside the CNA to the northeast direction of CNA. The whole process of finishing a round trip took 70 seconds. White dash line indicates the full itinerary of laser movement and red arrow shows the laser moving direction during the corresponding frame.

depicts tighter trapping stability for the same exosome trapped in site II *versus* when the exosome was trapped in site I. We also note that the enhanced trapping stability in site II can be tuned by controlling the width of the gap region defined by site II. We have varied the width of the gap region of site II using widths of (6, 10 and 20  $\mu\text{m}$ ) and show a narrower gap width provides stronger trapping stability on the trapped exosomes as detailed in Fig. S4 of the ESI section.†

After the single small exosome is loaded into site II, we demonstrate dynamic manipulation by moving the laser spot. As shown in Fig. 4, we begin with the laser spot close to the center of CNA and the exosome is in the northeast of the gap. Then, the laser spot moves a round trip across the inner circular pattern along ‘center  $\rightarrow$  south  $\rightarrow$  northwest  $\rightarrow$  northeast  $\rightarrow$  southeast’ direction. The white dashed curve depicts the trajectory of the laser motion. The corresponding video is provided in ESI video 3.† In the video, it took about 70 seconds to finish the whole manipulation process and the small exosome faithfully followed the motion of laser to complete the round trip, while the large exosome stayed to the northeast (circled in orange) of the CNA during the whole process. The dynamic manipulation is primarily enabled by the ETP flow. In site II, the distance to laser spot is shorter and the local ETP velocity will be higher. This ensures that the trapped exosomes in site II is within the radius of influence of the ETP flow to be dynamically manipulated by the ETP flow. Hence, the CNA system provides the means to achieve the selective manipulation of single exosomes.

## Conclusion

We have demonstrated a concentric nanohole array system for opto-thermo-electrohydrodynamic trapping, dynamic manipulation, and sorting of single nanoscale exosomes with high stability within seconds using low particle concentrations. The CNA system features selective trapping and selective dynamic manipulation of single exosomes based on size. Our proposed platform may be combined with other single molecule analysis techniques such as Forster Resonance Energy Transfer (FRET) by enabling to stabilize single exosomes in solution within a microscope observation volume without tethering to surfaces. Other analysis methods, such as surface enhanced Raman

spectroscopy (SERS), may also be supported with the CNA platform. By integrating plasmonic cavities at the electrohydrodynamic trapping positions,<sup>7</sup> CNA offers the opportunity for studying the chemical composition of nanoparticles, and sorting particles with desired composition for further analysis. The ability to trap and manipulate individual bioparticles selectively opens the door to single vesicle analysis to understand the heterogeneity of extracellular vesicles on the single-particle level.

## Author contributions

C. H. performed the fabrication and conducted the experiments. S. Y. and C. H. performed the numerical simulations. J. C. N. and C. H. discussed on the results and prepared the manuscript. J. C. N. conceived and supervised this project.

## Conflicts of interest

There are no conflicts to declare.

## Acknowledgements

The authors acknowledge support from NSF CAREER Award (NSF ECCS 2143836).

## Notes and references

- 1 Y. Li, X. Liu and B. Li, *Light Sci. Appl.*, 2019, **8**, 61.
- 2 J.-A. Huang, M. Z. Mousavi, Y. Zhao, A. Hubarevich, F. Omeis, G. Giovannini, M. Schütte, D. Garoli and F. De Angelis, *Nat. Commun.*, 2019, **10**, 5321.
- 3 M. Kumemura, D. Collard, C. Yamahata, N. Sakaki, G. Hashiguchi and H. Fujita, *ChemPhysChem*, 2007, **8**, 1875–1880.
- 4 A. Ndao, L. Hsu, W. Cai, J. Ha, J. Park, R. Contractor, Y. Lo and B. Kanté, *Nanophotonics*, 2020, **9**, 1081–1086.
- 5 B. Lin, Y. Lei, J. Wang, L. Zhu, Y. Wu, H. Zhang, L. Wu, P. Zhang and C. Yang, *Small Methods*, 2021, **5**, 2001131.
- 6 M. Tayebi, Y. Zhou, P. Tripathi, R. Chandramohanadas and Y. Ai, *Anal. Chem.*, 2020, **92**, 10733–10742.
- 7 C. Hong and J. C. Ndukaife, ArXiv, 2023, DOI: [10.48550/arXiv.2302.07370](https://doi.org/10.48550/arXiv.2302.07370), Preprint.
- 8 G. Raposo and W. Stoorvogel, *J. Cell Biol.*, 2013, **200**, 373–383.
- 9 J. De Toro, L. Herschlik, C. Waldner and C. Mongini, *Front. Immunol.*, 2015, **6**, 203.
- 10 A. Zijlstra and D. di Vizio, *Nat. Cell Biol.*, 2018, **20**, 228–230.
- 11 H. Peinado, M. Alečković, S. Lavotshkin, I. Matei, B. Costa-Silva, G. Moreno-Bueno, M. Hergueta-Redondo, C. Williams, G. García-Santos, C. M. Ghajar, A. Nitadori-Hoshino, C. Hoffman, K. Badal, B. A. Garcia, M. K. Callahan, J. Yuan, V. R. Martins, J. Skog, R. N. Kaplan, M. S. Brady, J. D. Wolchok, P. B. Chapman, Y. Kang, J. Bromberg and D. Lyden, *Nat. Med.*, 2012, **18**, 883–891.
- 12 J. Lötvall, A. F. Hill, F. Hochberg, E. I. Buzás, D. di Vizio, C. Gardiner, Y. S. Gho, I. v. Kurochkin, S. Mathivanan,



- P. Quesenberry, S. Sahoo, H. Tahara, M. H. Wauben, K. W. Witwer and C. Théry, *J. Extracell. Vesicles*, 2014, **3**, 26913.
- 13 C. Liu, X. Xu, B. Li, B. Situ, W. Pan, Y. Hu, T. An, S. Yao and L. Zheng, *Nano Lett.*, 2018, **18**, 4226–4232.
- 14 H. Li, T. Huang, L. Lu, H. Yuan, L. Zhang, H. Wang and B. Yu, *ACS Sens.*, 2022, **7**, 1926–1935.
- 15 N. Ullah Khan, Z. Muhammad, X. Liu, J. Lin, Q. Zheng, H. Zhang, S. Malik, H. He and L. Shen, *Nano Lett.*, 2021, **21**, 5532–5539.
- 16 C. Y. Chiang and C. Chen, *J. Biomed. Sci.*, 2019, **26**, 1–10.
- 17 S. H. Hilton and I. M. White, *Sensor. Actuator. Rep.*, 2021, **3**, 100052.
- 18 E. Willms, C. Cabañas, I. Mäger, M. J. A. Wood and P. Vader, *Front. Immunol.*, 2018, **9**, 1.
- 19 A. Ashkin, J. M. Dziedzic, J. E. Bjorkholm and S. Chu, *Opt. Lett.*, 1986, **11**(5), 288–290.
- 20 A. Ashkin and J. M. Dziedzic, *Science*, 1987, **235**, 1517–1520.
- 21 Z. J. Smith, C. Lee, T. Rojalin, R. P. Carney, S. Hazari, A. Knudson, K. Lam, H. Saari, E. Lazaro Ibañez, T. Viitala, T. Laaksonen, M. Yliperttula and S. Wachsmann-Hogiu, *Citation*, 2015, **4**, 28533.
- 22 W. Lee, A. Nanou, L. Rikkert, F. A. W. Coumans, C. Otto, L. W. M. M. Terstappen and H. L. Offerhaus, *Anal. Chem.*, 2018, **90**, 48.
- 23 S. G. Kruglik, F. Royo, J.-M. Guigner, L. Palomo, O. Seksek, P.-Y. Turpin, I. Tatischeff and J. M. Falcón-Pérez, *Nanoscale*, 2019, **11**, 1661–1679.
- 24 J. Penders, A. Nagelkerke, E. M. Cunnane, S. V. Pedersen, I. J. Pence, R. C. Coombes and M. M. Stevens, *ACS Nano*, 2021, **15**, 18192–18205.
- 25 A. Blázquez-Castro, *Micromachines*, 2019, **10**(8), 507.
- 26 C. Hong, S. Yang and J. C. Ndukaife, *Nat. Nanotechnol.*, 2020, **15**, 908–913.
- 27 K. B. Crozier, *Light Sci. Appl.*, 2019, **8**, 35.
- 28 C. Bustamante, L. Alexander, K. Maciuba and C. M. Kaiser, *Annu. Rev. Biochem.*, 2020, **89**, 443–470.
- 29 Y. Zhang, C. Min, X. Dou, X. Wang, H. P. Urbach, M. G. Somekh and X. Yuan, *Light Sci. Appl.*, 2021, **10**, 59.
- 30 C. J. Bustamante, Y. R. Chemla, S. Liu and M. D. Wang, *Nat. Rev. Dis. Primers*, 2021, **1**, 1–29.
- 31 D. G. Kotsifaki, V. G. Truong and S. Nic Chormaic, *Appl. Phys. Lett.*, 2021, **118**(2), DOI: [10.1063/5.0032846](https://doi.org/10.1063/5.0032846).
- 32 S. Ghosh and A. Ghosh, *Sci. Robot.*, 2018, **3**, eaaq0076.
- 33 S. Ghosh and A. Ghosh, *Nat. Commun.*, 2019, **10**, 4191.
- 34 J. C. Ndukaife, A. V. Kildishev, A. G. A. Nnanna, V. M. Shalaev, S. T. Wereley and A. Boltasseva, *Nat. Nanotechnol.*, 2016, **11**, 53–59.
- 35 J. S. Donner, G. Baffou, D. McCloskey and R. Quidant, *ACS Nano*, 2011, **5**, 5457–5462.
- 36 T. W. Ebbesen, H. J. Lezec, H. F. Ghaemi, T. Thio and P. A. Wolff, *Nature*, 1998, **391**, 667–669.
- 37 A. Ramos, H. Morgan, N. G. Green and A. Castellanos, *J. Phys. D Appl. Phys.*, 1998, **31**, 2338–2353.
- 38 C. Hong, S. Yang, I. I. Kravchenko and J. C. Ndukaife, *Nano Lett.*, 2021, **21**, 4921–4927.
- 39 M. M. Hatlo and L. Lue, *Soft Matter*, 2008, **4**, 1582.
- 40 D. Yoo, T. W. Johnson, S. Cherukulappurath, D. J. Norris and S. H. Oh, *ACS Nano*, 2015, **9**, 10647–10654.
- 41 H. Im, S. H. Lee, N. J. Wittenberg, T. W. Johnson, N. C. Lindquist, P. Nagpal, D. J. Norris and S.-H. Oh, *ACS Nano*, 2011, **5**, 6244–6253.

